Fast converging iterative wavefront sensing for scatter compensation in multi-photon fluorescence microscopy

Journal of Physics: Photonics

OPEN ACCESS

RECEIVED
6 May 2025

REVISED
23 June 2025

ACCEPTED FOR PUBLICATION
1 July 2025

PUBLISHED
11 July 2025

PAPER

Fast converging iterative wavefront sensing for scatter compensation in multi-photon fluorescence microscopy

Kibum Nam[1,2], **Maria Borozdova**[1], **Jung-Hoon Park**[2,*] **and Alexander Jesacher**[1,*]

[1] Institute of Biomedical Physics, Medical University of Innsbruck, Innsbruck, Austria
[2] Department of Biomedical Engineering, Ulsan National Institute of Science and Technology (UNIST), Ulsan 44919, Republic of Korea
* Authors to whom any correspondence should be addressed.

E-mail: jh.park@unist.ac.kr and alexander.jesacher@i-med.ac.at

Keywords: adaptive optics, nonlinear microscopy, deep tissue imaging, two photon fluorescence microscopy, indirect wavefront sensing

Supplementary material for this article is available online

Abstract

Adaptive optics can increase the imaging depth of nonlinear scanning microscopy by compensating for wavefront aberrations introduced by the sample using a spatial light modulator. Recent developments focus on the compensation of multiple scattering for deep tissue imaging. In this regime, sensorless iterative wavefront measurement schemes are often used due to their simplicity and robustness. Recently, we proposed such an iterative scheme, which we named 'Dynamic Adaptive Scattering compensation Holography' (DASH), and an even more powerful variant for complex modulation, c-DASH. The concept of DASH has some advantages over other iterative wavefront sensing strategies: it works for any aberration strength and converges in fewer measurements. Here, we present several improvements to the DASH concept that further accelerate its convergence and increase its feasibility for arbitrary scattering strengths. We demonstrate the impact of our improvements through numerical simulations and two-photon excited fluorescence microscopy experiments on synthetic scattering masks and genetically labelled endothelial cells in a mouse lung tissue. In simulations, we further verify that the optimised c-DASH can find a correction pattern through all considered aberration modes in a little more than a single measurement iteration, making it one of the fastest converging iterative wavefront sensing methods available.

1. Introduction

The ability to observe individual cells and subcellular compartments deep within biological tissues is highly desirable but is hampered by the degrading effect of the tissue itself, which scatters photons and increasingly degrades the quality of microscopic images as one tries to image at deeper depths. Nonlinear scanning imaging techniques such as multi-photon excited fluorescence [1–8] and harmonic generation microscopy [9–12] show particularly high penetration depth, but even these methods are limited to fractions of a millimetre in most tissues [13–15]. A promising strategy to increase the imaging depth further is to apply active wavefront control on the excitation beam via a spatial light modulator (SLM), with the aim to counteract the light scattering imposed by the tissue. As direct wavefront sensors tend to fail beyond a certain degree of turbidity, a common approach for finding effective wavefront compensation shapes is to retrieve them indirectly through many subsequent test measurements while the focus is held on a particular position inside the tissue. A range of such wavefront sensorless procedures has been developed to this end, all aimed at finding effective wavefront compensation shapes in the shortest possible time and with the lowest possible photon energy dose to the tissue [16–18]. Most of these procedures rely on some sort of phase-stepping interferometry, where the excitation beam is split into a 'reference beam' and a 'test beam', which is phase-stepped to maximise the signal (usually multi-photon excited fluorescence or harmonic signal) generated in the focal volume. The concept originates from earlier multi-dither techniques aiming at compensating atmospheric turbulence [19].

Recently, some of us have developed one such strategy, which we refer to as 'Dynamic Adaptive Scattering compensation Holography' (DASH) [18]. In DASH, the SLM splits the excitation beam into plane test waves and a reference beam using digital phase holography. DASH has certain advantages compared to alternative techniques, such as fast convergence, high robustness, and simplicity of use. Furthermore, it is 'auto-aligning', i.e. an accurate alignment of the SLM to the objective pupil is not needed.

However, it also has some shortcomings. One is that the use of phase-only holography leads to inaccuracies in the shaping of fields [20], which prevents the method from exploiting its full potential. Recently, we addressed this issue by introducing 'complex DASH' (c-DASH) [21], which employs fully complex-valued digital holography. Another drawback of the original DASH version is that optical aberrations must be strong for the method to work optimally, i.e. a large proportion of the excitation light must be scattered into many different propagation angles. While this is obviously the target application for DASH, it would be desirable for the method to be equally effective in correcting for smaller aberrations, such as those that persist at shallow imaging depths or those introduced by the optical elements of the microscope (system aberrations).

In this article, we present improved versions of DASH and c-DASH, which not only maintain their performance across any scale of turbidity but also generally result in a faster signal increase and shorter correction times. This is essentially achieved by choosing more appropriate weightings for the incremental updates to the correction mask as the algorithm progresses. We further introduce an abort criterion, which makes the algorithms faster by only testing those modes that are essential for the correction. Our modifications lead to aberration corrections established in fewer measurements compared to the original DASH/c-DASH versions. For the optimised c-DASH, for example, we demonstrate that independent of the aberration strength, best possible corrections can be achieved in only a single iteration through all considered test modes, i.e. $3N$ measurements for N modes [22, 23], if a guide-star is present to guide the optimisation, and only little more than $3N$ measurements in case the guide-star assumption does not hold. We demonstrate the improved performance of DASH by numerical simulations and experimental two photon-excited fluorescence (TPEF) microscopy.

2. DASH principle

DASH describes the aberration-compensating excitation field on the objective pupil as a superposition of plane waves: $\sum_{m=1}^{N_m} w_m M_m$, where N_m represents the total number of plane waves included and M_m a particular plane wave (hereafter referred to as test beam or mode). DASH aims to find those complex-valued coefficients w_m that maximise the generated two-photon fluorescence signal $I_{2\mathrm{ph}}$ (figure 1(a)). This is achieved via holographically shaping each plane wave in turn, together with a reference field C_m consisting of the sum of all previously measured plane waves, normalised by a constant γ_m to have the same power as the plane wave M_m. When the plane waves M_m are sequentially tested, we sort them in ascending order with respect to their propagation angle to the optical axis. In DASH(phase-only modulation), the phase patterns shaped by the SLM hologram are calculated as:

$$\Phi_{\mathrm{SLM},m} = \mathrm{angle}\left(\sqrt{f}M_m + \sqrt{1-f}\frac{C_m}{\gamma_m}\right) \tag{1}$$

where the real-valued number f represents the power fraction contained in the test mode, because M_m and C_m/γ_m are normalised to equal power. Conversely, the variant c-DASH assumes that the full complex-valued field can be shaped:

$$U_{\mathrm{SLM},m} = \sqrt{f}M_m + \sqrt{1-f}\frac{C_m}{\gamma_m}. \tag{2}$$

In both methods, DASH and c-DASH, each plane wave is phase-stepped at least three times and the coefficient w_m retrieved via interferometry, which is immediately followed by an update of the reference field C:

$$C_{m+1} = C_m + w_m M_m \tag{3}$$

C_{m+1} acts as the new reference for measuring the coefficient of the following mode M_{m+1}. Following this scheme, the aberration correcting pattern, C is continuously improved. Of note, this pattern is a complex-valued quantity, i.e. it also contains information about amplitude aberrations or 'open channels' [24]. However, this information can only be utilised in c-DASH [21], while DASH can only display the phase part.

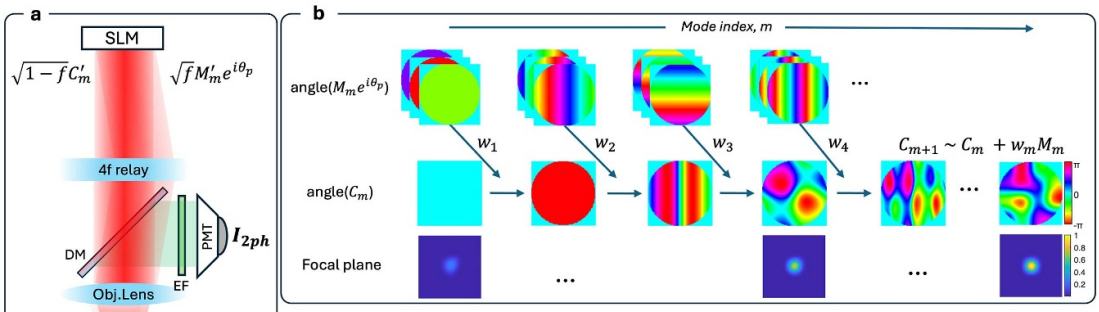

Algorithm	Measuring	$\lvert w_1\rvert$	$\lvert w_m\rvert, m > 1$
Original DASH	**Amplitude of the interference term**	0	$\sqrt{(1-f)f}\lvert M'_m\rvert\lvert C'_m\rvert$
Optimized DASH	**Contribution of current mode, M_m**	$\lvert M'_1\rvert$	$\lvert M'_m\rvert$

Figure 1. Principle. (a) A wavefront-corrected beam C'_m and a test beam M'_m are jointly shaped by the corresponding holograms C_m and M_m displayed on an SLM, which then arrive at the fluorophore inside the scattering media. Both beams interfere inside the scattering media where they generate two-photon excited fluorescence intensity $I_{2\mathrm{ph}}$. DM, dichroic mirror; EF, emission filter. (b) Principle of measuring $|w_m|$ in original DASH and optimised DASH. M'_m is phase-stepped to determine its optimal weight w_m, after which C_m is updated to $C_{m+1} = C_m + w_m M_m$. **Table**: Calculation of weight for a mode in original DASH and optimised DASH.

In the following, we derive the optimised DASH algorithm step by step, highlighting differences to the previously published version [18]. There are two main differences: Firstly, the mode weights w_m are calculated such that they more accurately estimate the power of the test mode at the focal point inside the scatterer. Secondly, we now make a more optimal assumption for the initial reference field C_1, i.e. the reference which interferes with the very first test beam M_1.

2.1. Derivation of original DASH

When focusing into an aberrating sample, measurable TPEF is generated by all fluorophores located in the vicinity of the nominal focal point. The contributions of all these sources can be described as a sum:

$$I_{2\mathrm{ph,\,tot}} = \sum_{s=1}^{N_s} I_{2\mathrm{ph},s}$$

where s is the source index and N_s the number of fluorescence sources. To enable an analytical treatment, we have to assume that one source dominates. In experiments, this is of course not necessarily true, at least not at the beginning of the correction routine, where the excitation focus light spreads out over a larger volume. However, in general one source contributes with the strongest signal, and our simple assumption will gain increasing validity as the algorithm progresses and a tight focus forms. We will later address the consequences of a violation of the 'single source' assumption in more detail. The TPEF generated by this dominating source (the 'guide star') can be described as:

$$I_{2\mathrm{ph},m}(p) = \sigma \left| \sqrt{1-f}\, C'_m + \sqrt{f}\, M'_m\, \mathrm{e}^{\mathrm{i}\theta_p} \right|^4. \tag{4}$$

Here, σ contains proportionality constants that link the physical light fields M'_m and C'_m with the detected TPEF power, such as fluorophore density, two-photon absorption cross section and collection efficiency. Since its actual value is irrelevant for the following considerations, we set it to one: $\sigma = 1$. It is worth highlighting the difference between the quantities M and C and its primed pendants M' and C'. While M and C are the numerical arrays on the computer which create proportional physical light fields through the SLM in the objective pupil, M' and C' represent the corresponding parts of these pupil light fields which actually arrive at the guide star inside the scattering tissue. The quantity θ_p is the phase offset imposed to M'_m when it is holographically shaped. Defining a signal quantity $S_m(p)$ as the square-root of the TPEF signal $\sqrt{I_{2\mathrm{ph},m}(p)}$, we can write:

$$\begin{aligned} S_m(p) &= \left| \sqrt{1-f}\, C'_m + \sqrt{f}\, M'_m \mathrm{e}^{\mathrm{i}\theta_p} \right|^2 \\ &= \bar{S}_m + \sqrt{f(1-f)} \left(C'_m\, M'^{*}_m \mathrm{e}^{-\mathrm{i}\theta_p} + C'^{*}_m\, M'_m \mathrm{e}^{\mathrm{i}\theta_p} \right) \end{aligned} \tag{5}$$

where $\bar{S}_m$ is the mean signal

$$\bar{S}_m = (1-f)\,|C'_m|^2 + f|M'_m|^2\,. \tag{6}$$

In our original implementation, the complex weight of the m-th test mode is retrieved by calculating the arithmetic average of all N_p phase-stepped signal measurements multiplied by their phasors:

$$a_m = \frac{1}{N_p}\sum_{p=1}^{N_p} S_m\,(p)\,\mathrm{e}^{\mathrm{i}\theta_p} = \sqrt{f(1-f)}|M'_m||C'_m|\mathrm{e}^{\mathrm{i}\varphi_m} \tag{7}$$

where φ_m is the phase difference between reference and test beam: $\varphi_m = \mathrm{angle}(C'_m) - \mathrm{angle}(M'_m)$. In our original DASH implementation, a_m was directly taken as the complex weight w_m in equation (3) and figure 1. However, from equation (7), we can see that the modulus of a_m depends not only on the mode magnitude $|M'_m|$, but also on the heuristically chosen parameter f and the reference field amplitude $|C'_m|$, which increases continuously during the algorithm as its aberration correction improves. This leads to a continuously increasing overestimation of the mode weights, which can slow down the convergence in some cases. In fact, this was already remarked in our first publication on DASH [18], but its significance was underestimated at the time.

2.2. Optimisation step 1: calculating optimal mode weights

To improve the performance of DASH, we therefore define the mode weight w_m as:

$$w_m = |M'_m|\mathrm{e}^{\mathrm{i}\varphi_m}. \tag{8}$$

The quantity $|M'_m|$ can be derived from the mean signal, $\bar{S}_m$ in equation (6) and the absolute square of the previous weight definition a_m in equation (7), which leads to the following squared equation:

$$|M'_m|^2 = \frac{\bar{S}_m}{2f} \pm \frac{1}{2f}\sqrt{\bar{S}_m^2 - 4|a_m|^2}. \tag{9}$$

The two solutions of this quadratic equation represent the intensities of the two interfering beams. We need to consider the smaller of the two solutions, because we have $f < 0.5$ and $|C'_m|$ continuously increases during the optimisation while $|M'_m|$ remains unchanged.

Therefore, the correct solution for the mode magnitude is:

$$|M'_m| = \sqrt{\frac{1}{2f}\left(\bar{S}_m - \sqrt{\bar{S}_m^2 - 4|a_m|^2}\right)}. \tag{10}$$

Finally, we can state a formula to calculate the complex weight w_m, based on the measured quantities $\bar{S}_m$ and a_m:

$$w_m = \sqrt{\frac{1}{2f}\left(\bar{S}_m - \sqrt{\bar{S}_m^2 - 4|a_m|^2}\right)}\,\mathrm{e}^{\mathrm{i}\ \mathrm{angle}(a_m)}. \tag{11}$$

As outlined at the beginning of this section, an underlying assumption of our derivation is the existence of a single guide star. This assumption is not fulfilled if the excitation beam spreads around the focus, exciting many fluorescent sources in its vicinity. In such cases, calculating the weights according to equation (11) will lead to an overestimation of the weights, because a significant portion of the detected signal will stem from other fluorescent sources than the guide star where the focus will form. In order to account for this effect, we may introduce a scalar factor $r_m \in [0, 1]$ to *decrease* the mode weights:

$$w_m = r_m|M'_m|\mathrm{e}^{\mathrm{i}\varphi_m}. \tag{12}$$

Finding suitable values for r_m would require prior knowledge about which fraction of the detected signal stems from the signal source at the future focal point. While such prior knowledge may not be available for entirely unknown samples, it is still possible to use a statistical estimate, for example based on a series of previous measurements at different focal points for the same sample.

2.3. Optimisation step 2: measuring the weight of the first mode

Apart from calculating the mode weights in a more optimal way, an improved versatility of DASH can be obtained by a second modification, which concerns the very first DASH measurement, where C_1' interferes with M_1'. In original DASH, C_1 is simply set to 1. Because the test modes are usually sorted in ascending order to their propagation angle, the first test mode M_1 represents a plane wave propagating in parallel to the optical axis and is therefore also equal to 1.

For DASH, however, any attempt to measure w_1 in the phase-stepping routine will result in $w_1 = 0$. The reason for this is explained as follows: When calculating the measurement holograms according to equation (1), we are essentially adding two identical fields (both being arrays of ones) with a mutual phase shift θ_p. This only produces global changes of amplitude and phase across the entire SLM hologram. Displaying only the phase part of this sum, as we do in DASH, has no effect at all on the generated TPEF signal. Therefore, the measured signal modulation amplitude will be zero and as a consequence, the reference field remains unchanged after the first measurement, i.e. $C_2 = C_1 = 1$. Of note, C_2 represents the zero-order Fourier component of the developing reference field, and setting it to 1 has no physical relation to the weights of the higher Fourier components $w_m, (m \geqslant 2)$, which are measured in the following DASH steps and depend on physical parameters such as the measured TPEF signal $I_{2\mathrm{ph}}$. For example, we usually operate our system in photon counting mode, in which case $I_{2\mathrm{ph}}$ usually takes values around $10^2 - 10^4$ photons. This leads to $w_m \gg 1$ for $m \geqslant 2$ in contrast to which the choice of a zero-order Fourier component of $C_2 = 1$ strongly underestimates that of a realistic scatterer. We observed that while this stark mismatch between the assumed and real strength of the compensation mask's zero-order Fourier component has no negative impact on the DASH performance when the aberrations are strong and a significant part of the energy is scattered into higher angles, such that many Fourier components are populated. However, it has severe negative effects for the case of weak aberrations or when the system is aberration-free; in such cases, it becomes more important that the magnitude of the zero-order Fourier component has a realistic relation to the higher Fourier components.

To understand this better, let us assume we run DASH for the aberration-free case. Here, we would expect all Fourier components of the correction pattern to be zero, except its DC component. Exactly this DC component, however, has been set to the comparatively small value of 1 and will be surpassed by even tiny light contributions that are measured at higher Fourier components. Consequently, DASH begins building up a correction mask that directs light into those higher angles, effectively scrambling the pupil phase. The algorithm will recover in later iterations, but this behaviour slows down the optimisation process and is clearly undesired.

To remedy this problem, we propose skipping the first phase-stepping set to determine w_1 and using a calculated value instead. In fact, w_1 can be derived from a single measurement: Since the interfering fields C_1' and M_1' are identical, the phase shift between them is zero and from equation (6) we see that $\bar{S}_1 = |C_1'|^2 = |M_1'|^2$, where $\bar{S}_1$ is the (square-rooted) TPEF signal when the SLM is left blank, i.e. no modulation is performed. From equation (12) we conclude:

$$w_1 = r_1 \sqrt{\bar{S}_1} \tag{13}$$

where r_1 has the same role to reduce the weight if the single guide-star assumption does not hold. Again, r_1 can be estimated from previous correction runs on the samples that have similar features of scattering. The two discussed optimisations lead to optimised DASH/c-DASH routines, which are outlined in the pseudo-code in the supplemental document.

3. Numerical simulations

We test the optimised DASH routine along with c-DASH in numerical simulations using Python and compare it to the original versions. For the simulations presented in this main text, we use a rather simple physical model. The simulation code is provided in our online repository [25]. Further simulation results based on a more realistic model are included in the supplemental document. The simple model assumes a square objective pupil sampled by 24×24 pixels. The SLM and the phase scatterers are both located in the objective lens pupil plane and sampled with the same resolution. The power ratio f for the test beam is fixed to $f = 0.2$. The number of test beams and the number of phase steps are set to 576 and 3, respectively. These parameters are applied to all the following simulations unless otherwise stated. A fluorescent sample is assumed in the focal plane of the objective lens and the two-photon signal is calculated as $I_{2\mathrm{ph}} = \sum \left(\mathrm{sample} \cdot |\mathrm{FFT}(U_{\mathrm{SLM}}\, \mathrm{e}^{i\,\Phi_{\mathrm{scat}}})|^4\right)$, where U_{SLM} is the light field shaped by the SLM and Φ_{scat} the random phase scatterer. The simulations do not include noise from photon statistics or the detection process. We normalise the two-photon signal such that $I_{2\mathrm{ph}} = 1$ for the aberration-free case.

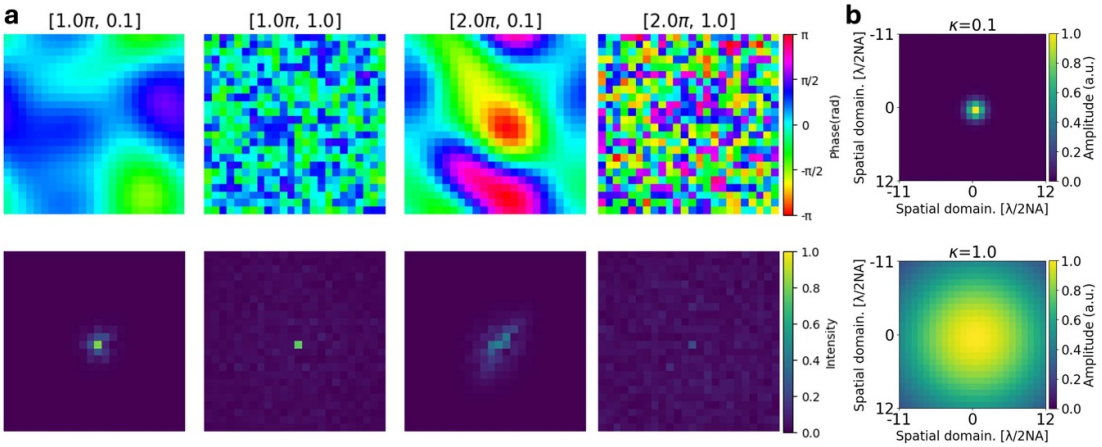

Figure 2. Defining artificial aberrations. (a) First row: Four random phase scatterers parametrised by two values: $[\Phi_{PV}, \kappa]$ which represents [peak-to-valley phase, spatial frequency control parameter]. Second row: intensity of initial PSFs of the optical system for the scatterers shown in the first row. (b) Gaussian low-pass spatial filters to control the spatial frequency of random phase masks. The parameter κ in the subtitles represents the ratio of the FWHM of the Gaussian filter to the width of the spatial domain.

3.1. Artificial aberrations

We define four different types of random phase scatterers to benchmark our algorithms, each differing their scattering characteristics. Each scatterer type is parametrised by its peak-to-valley phase Φ_{PV} and a parameter κ, which controls its spatial frequency content.

We first initialise a scatterer phase mask Φ_{scat} in the pupil plane by generating 24×24 uniformly distributed random phase values using the random function of the Python package *JAX*. The pattern is then low-pass filtered by applying a multiplicative Gaussian filter to the 2D FFT of Φ_{scat} whose domain corresponds to the focal plane (figure 2(b)). The parameter κ represents the FWHM of this Gaussian filter, stated in units of the size of the simulated spatial domain, which in our case is $12\frac{\lambda}{NA}$. Finally, the range of the random phase values is adapted to the user-defined value Φ_{PV}. We choose the following four parameter sets for the scatterers: $[\Phi_{PV}, \kappa] = [1.0\pi, 0.1], [1.0\pi, 1.0], [2.0\pi, 0.1], [2.0\pi, 1.0]$. These four different parameter sets are used throughout the simulations and experiments presented in this manuscript. Exemplary realisations of these four scatterer types are shown in the first row of figure 2(a).

3.2. Optimised DASH versus optimised c-DASH

First, we aim to verify the mathematical reasoning presented in section 2, test the implementation of the optimised DASH algorithm and its effectiveness, and compare it with optimised c-DASH. The simulations are performed for the aforementioned four scatterer types (figure 2), assuming a single guide star or a 2D homogeneous layer as the fluorescent sample in the focal plane. To increase the robustness of our conclusions, we ran simulations on five different random realisations for each scatterer type. The number of phase steps is set to the minimum value of 3.

The results are summarised in figure 3, which illustrates how the TPEF signal improves during the DASH and c-DASH routines. Each curve shows the average signal increase obtained when correcting for a particular scatterer, with the coloured bands showing the standard deviation. The horizontal green dashed line marks the signal obtained in the aberration-free case and the vertical red dashed lines mark the end of each iteration.

In general, higher Φ_{PV} values lead to weaker initial signals, while κ affects the slope. Since our algorithm analyses and corrects modes in ascending order based on their angle of propagation (spatial frequency), the signal can be recovered more quickly if only the lowest-order modes are scrambled ($\kappa = 0.1$), while correcting a high spatial frequency scatterer ($\kappa = 1$) requires all available modes for testing and correcting.

Independent of the aberration strength, c-DASH establishes full corrections after only a single iteration if a single guide star is present (see supplemental document). Even under the unfavourable condition of strong scattering combined with a homogenous fluorescent layer as sample, c-DASH requires only a little more than a single iteration. Under these conditions, DASH needs almost three iterations to converge. These results align well with the more realistic numerical simulations provided in the supplemental document, where the scatterer is modelled as a stack of axially separated phase masks.

The DASH optimisation can occasionally lead to a temporary signal *decrease*, here visible for the parameter pair $[2.0\pi, 0.1]$ for a short time during the first iteration. This can happen when modes are tested that are irrelevant for the correction, but a reasonably tight focus has not yet formed. In such cases, inaccurate estimates of the mode phases lead to an increase of the aberration magnitude and hence to a

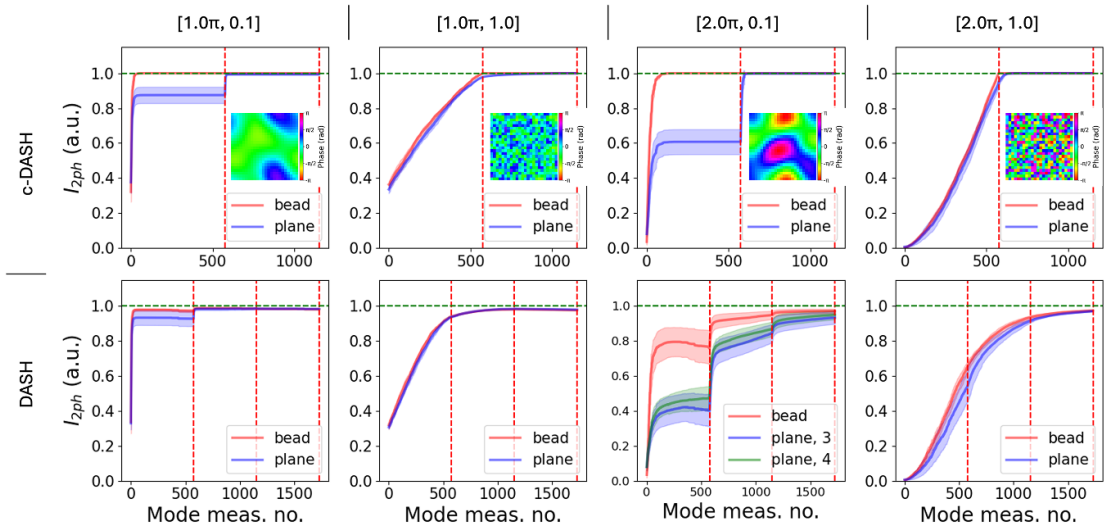

Figure 3. Two-photon fluorescence signal enhancement of optimised c-DASH and DASH applied to the four different scatterers assuming a single guide star ('bead') and 2D homogeneous fluorescent layer ('plane'). Each simulation was implemented five times with different random realisations of scatterers parametrised with $[\Phi_{\mathrm{PV}}, \kappa]$. The exemplary artificial aberrations for both algorithms are shown as insets. The average signal improvements and standard deviations are indicated by solid lines and ribbons, respectively. The legends show the type of fluorescent sample. The green and red dashed lines mark the ideal signal value (horizontal line) and the end of each iteration (vertical lines), respectively. Additional simulations with $N_p = 4$ are implemented for the case of '$[2.0\pi, 0.1]$, DASH, plane'. N_p is fixed to 3 for all the other simulations.

signal decrease. This can be remedied by running DASH using 4-phase steps (green plot), at least during the first iteration. In this case, any deviations from the cosine shape the signal is expected to take during phase stepping are less critical and the optimal phase correction can be more reliably found [21].

Note that all results shown in figure 3 have been obtained with $r_m = 1$. This means that our second proposed optimisation step discussed (equation (12)) has not yet been applied. In fact, the non-ideal choice of r_1 is partly responsible for the pronounced initial performance lag when optimising with the 'plane' sample compared to the 'bead' sample for the scatterer type $[2\pi, 0.1]$. Further information on optimising our algorithms by a suitable choice of r_1 can be found in the Supplementary document.

Besides the optimisation steps discussed in section 2, we propose another practical improvement: because a flattening of the signal curves already in the first iteration (occurring in the data of the first and third columns in figure 3) indicates that the most significant modes have already been corrected, we may introduce an abort criterion, allowing the current iteration to stop and the next to begin when the signal slope falls below a user-defined threshold. Unlike related techniques such as IMPACT [16, 26], where the number of modes to be corrected is predetermined, DASH allows for flexible adaptation to the scatterer's characteristics, enabling the shortest possible correction time. This advantage is shared with other techniques that use instantaneous updates, as demonstrated with Hadamard patterns [27]. Our experiments confirm that this threshold is particularly effective when the scatterer's spatial frequency is low. More information about the effectiveness of this abort criterion is provided in the supplemental document.

3.3. Optimised DASH versus original DASH

In this section, we finally investigate the effectiveness of our optimisations for DASH in comparison with the original version, because phase-only modulation is more practical and easier to implement in an experiment than c-DASH, which requires the ability for joint amplitude and phase modulation.

Figure 4 shows TPEF signal improvements when applying original and optimised DASH for compensating the four scatterer types of figure 2, under the assumptions of a single-pixel guide star ('bead') and a 2D homogeneous fluorescent layer ('plane') in the focal plane. For reliable conclusions, we ran simulations on five different random realisations for each scatterer type. The mean intensity and standard deviation are shown as solid lines and coloured bands, respectively.

The original DASH version struggles particularly with weak scatterers (first two columns in figure 4), where an incorrectly assumed magnitude of the zero-order Fourier component (normal plane wave) of the scatterer has a strong negative impact. Conversely, for the strong scatterers (last two columns in figure 4), original DASH performs almost equivalent to optimised DASH. Our optimisations are therefore most effective if only mild aberrations are present, which cause only little stray light in close vicinity to the focus.

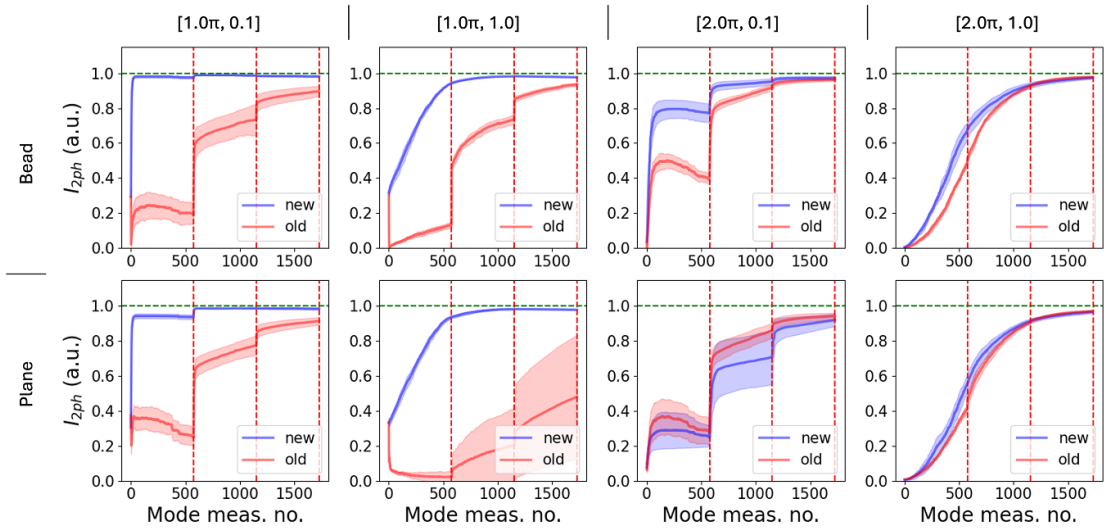

Figure 4. Comparison of original and optimised DASH. TPEF signal enhancements achieved by original ('old', red) and optimised DASH ('new', blue) for the cases of a single pixel guide star ('bead') and a 2D fluorescent layer ('plane') in the focal plane, under 4 different random realisations of scatterers parametrised with $[\Phi_{PV}, \kappa]$. Each simulation was executed five times. The average signal improvements and standard deviation are represented by solid lines and ribbons, respectively. The green and red dashed lines mark the ideal signal value (horizontal line) and the end of each iteration (vertical lines), respectively.

Of note, all the simulations shown in figure 4 assume $r_m = 1$, which means that further improvements are possible as discussed previously.

4. Experimental results

In our numerical simulations, we have shown that our optimisation steps significantly improve both algorithms, DASH and c-DASH. We now focus on demonstrating these improvements in TPEF experiments. While c-DASH promises the best performance, it is not easy to implement without prohibitive losses [21]. Therefore, we will only experimentally investigate phase-only DASH.

To experimentally verify our DASH optimisation, we built a custom two-photon microscope (TPM) (figure 5) incorporating a pulsed femtosecond laser (Mai Tai DeepSee®, MKS Spectra-Physics), x & y galvanometric scanners (Galvos), a segmented deformable mirror (492-3.5-SLM, Boston Micromachines) and a liquid crystal-based SLM (HSP1920, Meadowlark Optics). Both SLMs (hereafter referred to as DM and LC-SLM) and Galvos are conjugated to the pupil plane of the objective lens (20×, 1.0 NA, Olympus XLUMPLFLN water immersion). The DM consists of 492 actuators arranged in an octagonal shape and is used to correct optical aberrations, while the LC-SLM is used to introduce artificial aberrations. The active pixel area of the DM is 4f-relayed to lie within that of the LC-SLM. Details to their alignment are provided in the supplemental document. The fluorescence emission from the sample is collected by the same objective and detected by a photomultiplier tube (PMT, Hamamatsu Photonics). The detection path includes a dichroic mirror (DMLP735B, Thorlabs) and a multi-photon emission filter (MF525-39, Thorlabs) that filters out the reflected excitation beam.

The control parameters for optimised DASH and original DASH for all experiments are set the same as the simulations except the number of phase steps and the number of iterations: The power ratio f for the test beam and the number of test beams are set to 0.2 and 576, respectively. The number of phase steps N_p for the experimental data has been increased from three to five, to mitigate the impact of noise.

4.1. Correcting artificial aberrations

The fluorescent sample was prepared by applying a green highlighter (excitation wavelength: 800 nm) to a glass slide, which was then covered with a thin coverslip of 100 μm thickness. This resulted in a thin layer of dye with an estimated thickness of several μm, which is a reasonable approximation of a '2D fluorescent layer'. Prior to the experiments, we first obtained a phase correction mask to compensate for system aberrations with the DM. The LC-SLM was left blank during this measurement. This correction mask was added as an offset to the DM in all the following measurements for correcting artificial aberrations.

We then used the LC-SLM to introduce artificial aberrations, using the same parameters as in the simulations and ran both original DASH and optimised DASH for each of the four artificial scatterers. The

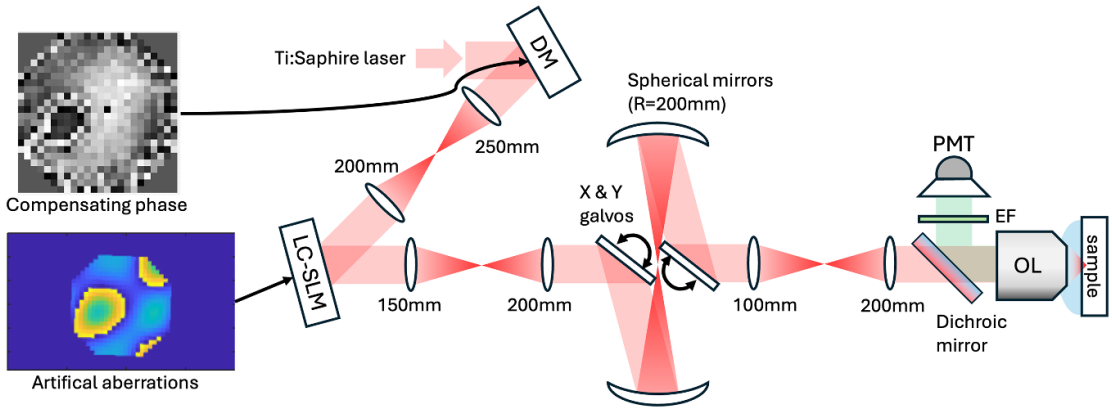

Figure 5. Two-photon microscope to implement DASH for compensating artificial and sample-induced aberrations. The artificial aberrations are introduced by a phase mask displayed on the LC-SLM and the DM is used to measure and correct them. A blank phase is loaded on LC-SLM when DASH corrects sample-induced aberrations. DM, deformable mirror; LC-SLM, liquid crystal SLM; PMT, photomultiplier tube; EF, emission filter; OL, objective lens. The DM and LC-SLM are conjugated to the pupil plane of the OL.

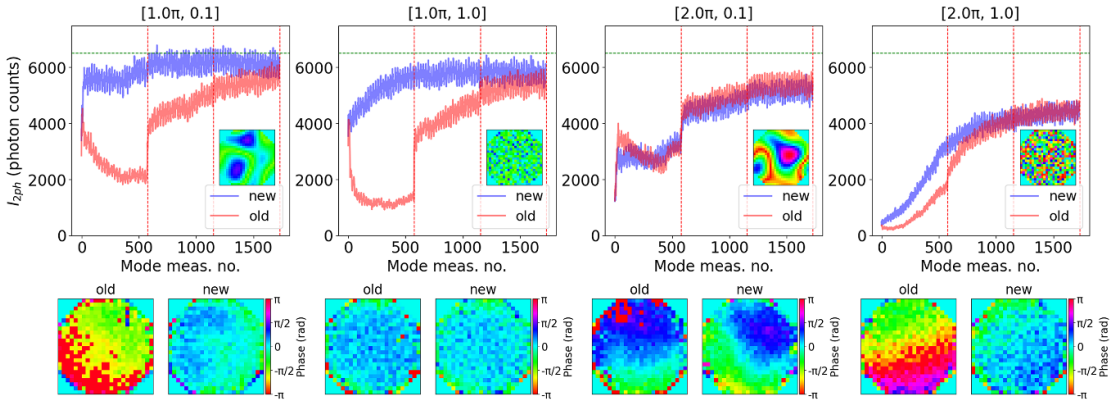

Figure 6. Experimental two-photon signal enhancements by original ('old') and optimised ('new') DASH compensating the four random scatterers for a 2D fluorescent layer. The subtitles of each graph represent the parameters $[\Phi_{PV}, \kappa]$ for each scatterer. The matching phase masks displayed on the LC-SLM are shown as insets. The horizontal green dashed lines mark the signal value measured for the aberration-free case (6500 photon counts). The end of each iteration is marked with vertical red dashed lines. The number of phase steps, N_p, is five. The achieved phase corrections are shown below. Each mask shows the sum of the respective aberration phase and the measured correction.

results are shown as four graphs of $I_{2\mathrm{ph}}$ in figure 6. A comparison of these four graphs with their corresponding simulation counterparts in the second row of figure 4 shows a very good match. The pupil phase corrected by original DASH tends to have a tilted wavefront, while optimised DASH has less of this tendency. This is a consequence of the underestimated zero-order Fourier component of the correction mask in original DASH, which effectively leads to a dominant off-axis mode and therefore a wavefront tilt.

A difference to the simulation is that the obtained signal levels after correction are smaller than those for the aberration-free case. This effect can be predominantly attributed to the limited diffraction efficiency of the LC-SLM, which we use to display aberration patterns. It is known that this efficiency drops with increasing spatial frequency of the displayed phase pattern.

In addition, we integrated optional functions, such as the possibility to adjust the weight of the first mode (equation (13)) and the activation of an abort criterion (discussed in the last paragraph of section 3.2) to demonstrate the possibility of improving DASH further. Details about the effectiveness of these additionally optimised measurements are provided in the supplemental document.

4.2. Correcting aberrations in mouse lung tissue imaging

So far, we have verified the optimisation of DASH using artificial aberrations in both simulations and experiments. To evaluate the feasibility of our optimised DASH for imaging applications, we prepared mouse lung tissue from a transgenic mouse (RRID:IMSR_JAX:007 896) that expresses GFP in its endothelial cells.

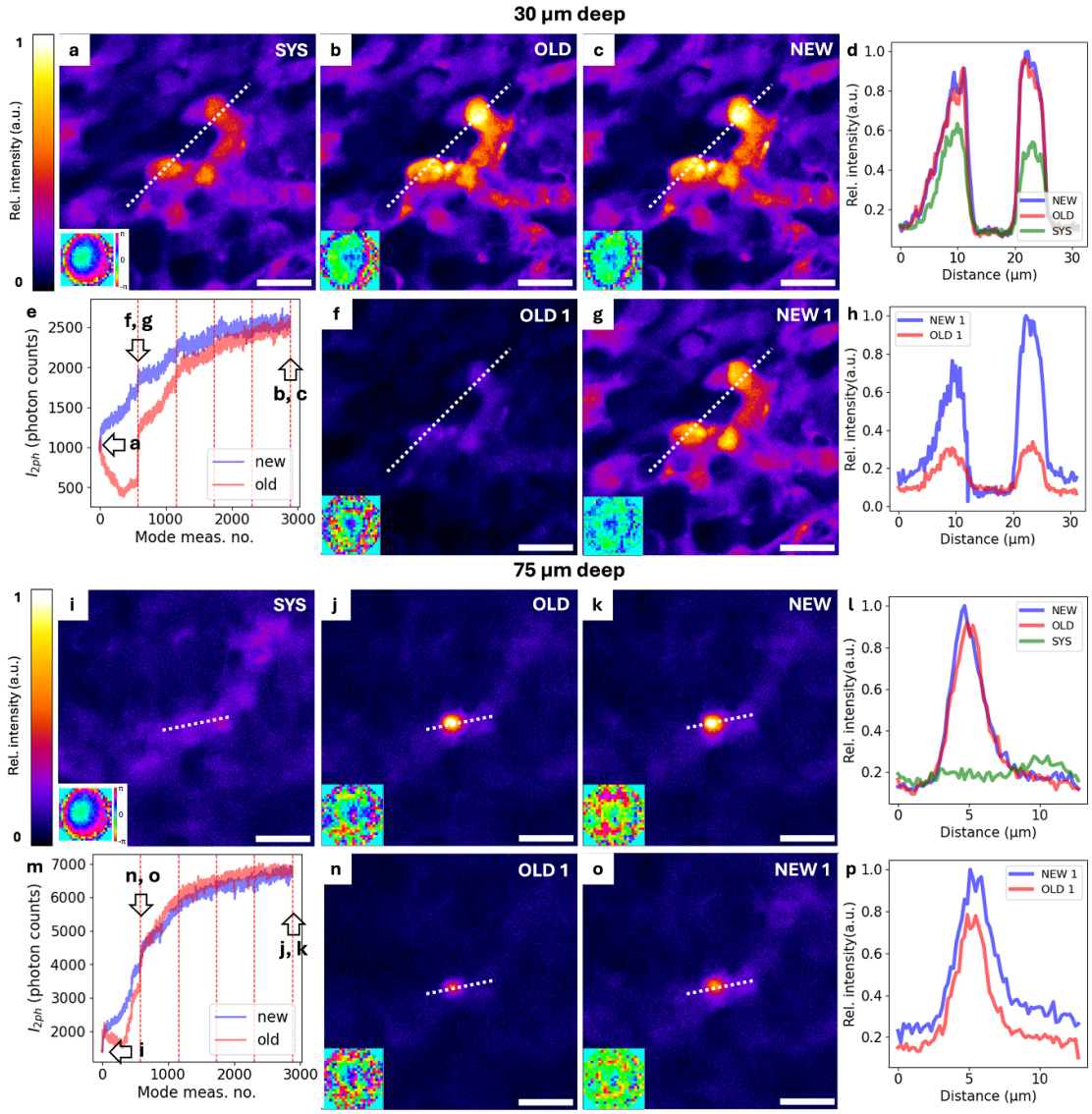

Figure 7. Wavefront corrections with original ('old') and optimised ('new') DASH for two-photon imaging of GFP-expressing endothelial cells in mouse lung tissue. Two-photon images of endothelial cells in mouse lung tissue at 30 μm depth ((a)–(c), (f)–(g)) and 75 μm ((i)–(k), (n)–(o)) depth from the surface. All the images for each depth are normalised to the maximum value. (e) and (m) Two-photon signal enhancements by 'old' and 'new' DASH implemented for the central region of the images. The images of the tissue are captured before correction ((a) and (i) only system aberration correction mask applied), after one iteration of 'old' ((f), (n)) and 'new' ((g), (o)) DASH, and after five iterations of 'old' ((b), (j)) and 'new' ((c), (k)) DASH. Line profiles of (a)–(c), (f)–(g), (i)–(k) and (n)–(o) are plotted in (d), (h), (l) and (p), respectively. Each plot is normalised to its maximum intensity. The image insets show the phase masks used for imaging. All phase masks use the same scale, as shown in the colourbar ((a) and (i)). The scale bars in all images represent 10 μm.

The lung tissue was placed in a Petri dish with phosphate-buffered saline and covered with a coverslip for imaging with the upright-positioned water immersion objective lens of the TPM.

Prior to applying original and optimised DASH on the tissue, we set the excitation wavelength to 900 nm, applied a blank phase mask to the LC-SLM and ran DASH on fluorescent debris located just beneath the coverslip to obtain the system aberration correction phase mask (insets in figures 7(a) and (i)). This system correction mask was then used as an offset for both original and optimised DASH.

To demonstrate the correction of relatively weak aberrations, the imaging depth was chosen to be 30 μm from the surface (figures 7(a)–(h)) and both 'old' DASH and optimised ('new') DASH were implemented to correct the aberrations. The two-photon signal enhancements obtained using both methods are depicted in figure 7(e). Both algorithms saturate to the maximum intensity after five iterations and provide near-identical correction phase masks and improved images (figures 7(b) and (c)). The final intensities are the same within the experimental noise level (figure 7(d)). However, as observed in both simulations and experiments with the artificial aberrations, 'old' DASH struggles to find proper weights for test modes in the

first iteration, while 'new' DASH continuously increases the signal. This difference is clearly observed in images taken after the first correction iteration (figures 7(f)–(h)).

For introducing relatively strong aberrations, the imaging depth was increased to 75 μm (figures 7(i)–(p)). The signal enhancements by 'old' and 'new' DASH are shown in figure 7(m). Again, both algorithms converge after five iterations and achieve equivalent correction masks and improved images (figures 7(j) and (k)). A visible consequence of the strong scattering is that the isoplanatic patch is small. The signal is only enhanced near the central region, while the surrounding areas show less signal compared to the image with only the system correction applied (figure 7(l)).

Although the differences between the signal enhancement plots (figure 7(m)) of 'old' and 'new' DASH are less pronounced than for the weak aberration case (figure 7(e)), 'old' DASH still shows a transient signal drop during the first iteration (figures 7(n)–(p)). We note that for 'old' DASH, similar signal drops are observed when the artificial aberrations are corrected, except for the strongly scattering case $[\Phi_{\mathrm{PV}}, \kappa] = [2.0\pi, 1.0]$. This indicates that the scattering caused by 75 μm thick lung tissue is still mostly forward-directed, which can also be inferred from the structure of the correction masks, where adjacent phase pixels in the centre are still highly correlated. Our observation is consistent with the fact that light scattering in biological tissue is predominantly forward directed [28, 29] and shows that our 'new' DASH implementation has superior performance to the original DASH in practical two-photon imaging applications.

5. Discussion on the speed of indirect wavefront measurements

When discussing the performance of iterative wavefront sensing methods, such as DASH or c-DASH, different performance figures may be considered. On the one hand, there is the actual measurement speed, or the time taken to retrieve a wavefront. Another performance figure is the number of test measurements required, which quantifies the efficiency of a method or the number of photons detected to complete a measurement. Although these two properties are related, they are not identical. DASH, and c-DASH in particular, excel in the latter, mostly due to the fact that the methods update the correction pattern immediately after each mode measurement. Simulations have shown that c-DASH requires only slightly more than a single iteration through all considered test modes for an almost full correction, whereas other methods usually require two or three iterations [16, 17, 30]. For the DASH experiments shown here, the typical correction time was a few seconds per iteration. However, times well below a second should be achievable if the control loop is optimised. However, DASH and c-DASH are not necessarily the fastest methods as a small amount of computation is required between displaying successive holograms on the SLM, which also needs to switch quickly. For example, the related technique F-SHARP [17] requires a larger photon budget than DASH [18], but may allow for a faster implementation because its speed is practically independent of the SLM frame rate and fast galvo-based or acousto-optic scanning can be employed. Recently, a parallelised version of F-SHARP named *multiplexing digital focus sensing and shaping (MD-FSS)* [31] was reported to achieve correction times as short as 0.1 s using acousto-optical beam modulation and frequency multiplexing, based on two-photon fluorescence signals. However, this speed comes at the cost of higher technical complexity. For any method, the achievable correction times depend strongly on the signal flux, which can vary strongly depending on which fluorescent label is used. Of note, if strong laser signals can be used as feedback instead of weak fluorescent signals, corrections can be faster by orders of magnitudes. For example, the correction of 100 modes in as little as 100 s has been demonstrated using acousto-optical beam modulation [32].

6. Summary

We have presented optimised versions of c-DASH and phase-only DASH, two indirect wavefront sensing techniques for scatter compensation in multi-photon microscopy.

Our improvements include several measures: First, we propose an accurate calculation of the mode amplitude weights. We show that a careful choice of the very first mode weight is particularly important. Second, we discuss an adaptation of our algorithm that can be beneficial when the single guide star assumption is not fulfilled. We propose to use reduced mode weights to account for the fact that a certain fraction of the detected TPEF signal stems from other, weaker sources than the dominant one, where the focus will form. Finally, we introduce an abort criterion that stops the current iteration and immediately starts the next one if the slope of the signal improvement falls below a user-defined threshold. This avoids fruitless testing of modes that are irrelevant to the current scatterer compensation and hence to shorter correction times. We investigated the efficiency of our modifications using numerical simulations, finding that they do indeed lead to faster signal enhancement. The improvements are particularly effective when smaller aberrations need to be corrected.

In simulations, we find that optimised c-DASH requires only a single optimisation iteration to provide full corrections if a single guide star is present, and that this performance is independent of the strength of the scatterer. Furthermore, c-DASH requires only a little more than a single iteration even when the sample consists of a homogeneous fluorescent plane, which is known to challenge indirect wavefront sensing approaches. We could confirm this behaviour in more realistic numerical simulations, where the scatterer is modelled by a set of 2D phase layers in the focal volume. This property makes our optimisation of c-DASH routine one of the fastest converging indirect wavefront sensing techniques available, however, a power-efficient experimental implementation of c-DASH is still lacking [21].

We have further confirmed the effectiveness of optimised phase-only DASH in TPEF experiments. We performed a quantitative study by displaying controlled scattering masks with user-defined properties on an LC-SLM and compensating them by running DASH using a segmented deformable mirror with 492 actuators (DM). The experimental results are in good agreement with the simulations. Finally, we experimentally demonstrated phase-only DASH for biological TPEF imaging of GFP-expressing endothelial cells in mouse lung tissue. The results indicate that our improvements make DASH more suitable for practical TPEF imaging.

Data availability statement

The data that support the findings of this study are openly available at the following URL/DOI: https://github.com/PrintRind/DASH.

Acknowledgments

The authors thank Mario Marini and Giorgio Meroni for their support for collecting the images of the murine tissue and Eva Ernst for scientific discussions.

Funding

This research was supported by the following research Grants: Korea Health Technology R&D Project through the Korea Health Industry Development Institute (KHIDI), funded by the Ministry of Health & Welfare, Republic of Korea (Grant No. HI19C1095); Bio & Medical Technology Development Program of the National Research Foundation (NRF) funded by the Korean government (MSIT) (No. RS-2024-00411768); Austrian Science Fund (10.55776/P36687).

Conflicts of interest

The authors declare no conflicts of interest.

References

[1] König K 2000 *J. Microsc.* **200** 83
[2] Denk W, Strickler J H and Webb W W 1990 *Science* **248** 73
[3] Hell S W, Bahlmann K, Schrader M, Soini A, Malak H M, Gryczynski I and Lakowicz J R 1996 *J. Biomed. Opt.* **1** 71
[4] Miller D R, Jarrett J W, Hassan A M and Dunn A K 2017 *Curr. Opin. Biomed. Eng.* **4** 32
[5] Xu C, Zipfel W, Shear J B, Williams R M and Webb W W 1996 *Proc. Natl Acad. Sci.* **93** 10763
[6] Xu C, Nedergaard M, Fowell D J, Friedl P and Ji N 2024 *Cell* **187** 4458
[7] Xu C and Zipfel W R 2015 *Cold Spring Harbor Protocols* **2015** db
[8] Zipfel W R, Williams R M and Webb W W 2003 *Nat. Biotechnol.* **21** 1369
[9] Aghigh A, Bancelin S, Rivard M, Pinsard M, Ibrahim H and Légaré F 2023 *Biophys. Rev.* **15** 43
[10] Chen X, Nadiarynkh O, Plotnikov S and Campagnola P J 2012 *Nat. Protocols* **7** 654
[11] Friedl P, Wolf K, Harms G and von Andrian U H 2007 *Curr. Protocols Cell Biol.* **34** 4
[12] Masihzadeh O, Schlup P and Bartels R A 2010 *Opt. Express* **18** 9840
[13] Takasaki K, Abbasi-Asl R and Waters J 2020 Superficial bound of the depth limit of two-photon imaging in mouse brain *Eneuro* **7** ENEURO.0255-19.2019
[14] Wang T, Wu C, Ouzounov D G, Gu W, Xia F, Kim M, Yang X, Warden M R and Xu C 2020 *Elife* **9** e53205
[15] Weisenburger S *et al* 2019 *Cell* **177** 1050
[16] Tang J, Germain R N and Cui M 2012 *Proc. Natl Acad. Sci.* **109** 8434
[17] Papadopoulos I N, Jouhanneau J S, Poulet J F and Judkewitz B 2017 *Nat. Photon.* **11** 116
[18] May M A, Barré N, Kummer K K, Kress M, Ritsch-Marte M and Jesacher A 2021 *Nat. Commun.* **12** 4340
[19] Bridges W, Brunner P, Lazzara S, Nussmeier T, O'Meara T, Sanguinet J and Brown J W 1974 *Appl. Opt.* **13** 291
[20] Sohmen M, May M A, Barré N, Ritsch-Marte M and Jesacher A 2022 *Front. Phys.* **10** 884053
[21] Sohmen M, Borozdova M, Ritsch-Marte M and Jesacher A 2024 *Phys. Rev. Appl.* **22** 044036
[22] Facomprez A, Beaurepaire E and Débarre D 2012 *Opt. Express* **20** 2598

[23] Booth M J 2006 *Opt. Lett.* **32** 5
[24] Davy M, Shi Z, Park J, Tian C and Genack A Z 2015 *Nat. Commun.* **6** 6893
[25] Jesacher A 2025 DASH *DASH simulation code* (available at: https://github.com/PrintRind/DASH)
[26] Park J H, Sun W and Cui M 2015 *Proc. Natl Acad. Sci.* **112** 9236
[27] Mastiani B and Vellekoop I M 2021 *Opt. Express* **29** 17534
[28] Jacques S L 2013 *Phys. Med. Biol.* **58** R37
[29] Jin H, Hwang B, Lee S and Park J H 2021 *Optica* **8** 428
[30] Rauer B, de Aguiar H B, Bourdieu L and Gigan S 2022 *Opt. Lett.* **47** 6233
[31] She Z, Fu Y, He Y, Yan G, Wu W, Qin Z and Qu J 2025 *bioRxiv Preprint* (https://doi.org/10.1101/2025.05.26.656230)
[32] Feldkhun D, Tzang O, Wagner K H and Piestun R 2019 *Optica* **6** 72